Fully gapped superconductivity and topological aspects of the noncentrosymmetric superconductor TaReSi

T. Shang,[1,2,*] J. Z. Zhao,[3,†] Lun-Hui Hu,[4] D. J. Gawryluk,[5] X. Y. Zhu,[1] H. Zhang,[1] J. Meng,[1] Z. X. Zhen,[1] B. C. Yu,[1] Z. Zhou,[6] Y. Xu,[1] Q. F. Zhan,[1] E. Pomjakushina,[5] and T. Shiroka[7,8]

[1]*Key Laboratory of Polar Materials and Devices (MOE), School of Physics and Electronic Science, East China Normal University, Shanghai 200241, China*

[2]*Chongqing Key Laboratory of Precision Optics, Chongqing Institute of East China Normal University, Chongqing 401120, China*

[3]*Co-Innovation Center for New Energetic Materials, Southwest University of Science and Technology, Mianyang 621010, China*

[4]*Department of Physics and Astronomy, University of Tennessee, Knoxville, Tennessee 37996, USA*

[5]*Laboratory for Multiscale Materials Experiments, Paul Scherrer Institut, CH-5232 Villigen PSI, Switzerland*

[6]*Key Laboratory of Nanophotonic Materials and Devices & Key Laboratory of Nanodevices and Applications, Suzhou Institute of Nano-Tech and Nano-Bionics (SINANO), CAS, Suzhou 215123, China*

[7]*Laboratory for Muon-Spin Spectroscopy, Paul Scherrer Institut, CH-5232 Villigen PSI, Switzerland*

[8]*Laboratorium für Festkörperphysik, ETH Zürich, CH-8093 Zürich, Switzerland*

(Received 8 September 2022; revised 19 May 2023; accepted 26 May 2023; published 8 June 2023)

We report a study of the noncentrosymmetric TaReSi superconductor by means of the muon-spin rotation and relaxation (μSR) technique, complemented by electronic band-structure calculations. Its superconductivity, with $T_c = 5.5$ K and upper critical field $\mu_0 H_{c2}(0) \sim 3.4$ T, was characterized via electrical-resistivity and magnetic-susceptibility measurements. The temperature-dependent superfluid density, obtained from transverse-field μSR, suggests a fully gapped superconducting state in TaReSi, with an energy gap $\Delta_0 = 0.79$ meV and a magnetic penetration depth $\lambda_0 = 562$ nm. The absence of a spontaneous magnetization below T_c, as confirmed by zero-field μSR, indicates a preserved time-reversal symmetry in the superconducting state. The density of states near the Fermi level is dominated by the Ta- and Re-5*d* orbitals, which account for the relatively large band splitting due to the antisymmetric spin-orbit coupling. In its normal state, TaReSi behaves as a three-dimensional Kramers nodal-line semimetal, characterized by an hourglass-shaped dispersion protected by glide reflection. By combining nontrivial electronic bands with intrinsic superconductivity, TaReSi is a promising material for investigating the topological aspects of noncentrosymmetric superconductors.

DOI: 10.1103/PhysRevB.107.224504

I. INTRODUCTION

In crystalline solids, a suitable combination of space, time-reversal, and parity symmetries often gives rise to exotic quasiparticles, analogous to the particles predicted in high-energy physics, such as Dirac, Weyl, or Majorana fermions [1–8]. In particular, materials which lack an inversion center are among the best candidates for studying topological phenomena, since most of them also exhibit nonsymmorphic symmetry that can often generate unusual types of fermionic excitations. For instance, Weyl fermions were experimentally discovered as quasiparticles in noncentrosymmetric tantalum and niobium pnictides [9–12]. Noncentrosymmetric materials can also host exotic fermions with an hourglass-shaped dispersion protected by glide reflection [13–15], which are known to exhibit interesting topological properties. In addition, Kramers nodal-line (KNL) fermions were recently forecasted to occur in noncentrosymmetric metals with a sizable spin-orbit coupling (SOC) [16,17]. To date, research on topological materials has been primarily focused on the case of noninteracting electronic bands. On the contrary, the interplay between topology and correlated electronic states, such as superconductivity (SC) or magnetism, remains largely unexplored.

Many noncentrosymmetric topological materials also exhibit superconductivity and, in view of their structure, are known as noncentrosymmetric superconductors (NCSCs). In NCSCs, the antisymmetric spin-orbit coupling (ASOC) allows, in principle, the occurrence of admixtures of spin-singlet and spin-triplet superconducting pairing, whose degree of mixing is generally believed to be determined by the strength of ASOC [18–20]. This sets the scene for a variety of exotic superconducting properties, e.g., nodes in the energy gap [21–24], multigap SC [25], upper critical fields beyond the Pauli limit [26–28], and breaking of time-reversal symmetry (TRS) in the superconducting state [24,29–35].

Noncentrosymmetric superconductors also provide a fertile ground in the search for topological SC and Majorana zero modes, with potential applications to quantum computation [36–43]. Among the many routes attempted to realize it, one approach consists in combining a conventional *s*-wave superconductor with a topological insulator to form a heterostructure. The proximity effect between the resulting

*Corresponding author: tshang@phy.ecnu.edu.cn
†Corresponding author: jzzhao@swust.edu.cn

surface states can lead to an effective two-dimensional SC with $p + ip$ pairing, known to support Majorana bound states at the vortices [44–46]. One can also consider introducing extra carriers (e.g., via chemical doping) into a topological insulator to achieve topological superconductivity [47,48]. A more elegant and clean route to attain topological SC is that of combining nontrivial electronic bands with intrinsic superconductivity in the same compound [49]. Some of the materials with nontrivial electronic band structures display topological surface states with spin-polarized textures [1–8]. When the bulk of the material transitions into the superconducting state, the proximity effect can give rise to topological superconducting surface states. Such protected surface states have been proposed, for instance, in noncentrosymmetric β-Bi_2Pd and $PbTaSe_2$ superconductors, both considered as suitable platforms for investigating topological SC [50,51]. Clearly, to pursue the "intrinsic" route, it is of fundamental interest to identify new types of superconductors with a nontrivial band topology.

Recently, NCSCs have become one of the most investigated superconducting classes due to their unconventional and topological nature. To this superconducting family belong also the TiFeSi-type materials, such as TRuSi and TReSi (with T a transition metal). The normal states of TaRuSi and NbRuSi are three-dimensional KNL semimetals, characterized by large ASOCs and by hourglass-like dispersions [52]. Both compounds spontaneously break the TRS in the superconducting state and adopt a unitary $(s + ip)$ pairing, reflecting a mixture of spin singlets and spin triplets. TaReSi also belongs to the TiFeSi family, and becomes a superconductor below 5.5 K [53]. Although certain properties of TaReSi have been previously investigated [54], its superconducting properties, in particular, the superconducting order parameter, have not been explored at a microscopic level. In this paper, by combining muon-spin relaxation and rotation (μSR) measurements with electronic band-structure calculations, we show that TaReSi exhibits a fully gapped superconducting state with a preserved TRS. It shares similar band topology with TaRuSi and NbRuSi, whose Kramers and hourglass fermions can easily be tuned toward the Fermi level by chemical substitutions. TaReSi serves as another candidate material for investigating the interplay between topological states and superconductivity.

II. EXPERIMENTAL DETAILS

Polycrystalline TaReSi samples were prepared by arc-melting stoichiometric Ta slugs (Alfa Aesar, 99.98%), Re powders (ChemPUR, 99.99%), and Si chunks (Alfa Aesar, 99.9999%) in a high-purity argon atmosphere. To improve sample homogeneity, the ingots were flipped and remelted more than six times. The resulting samples were then separated and annealed at 900 °C and 1100 °C for two weeks, respectively. An as-cast sample (denoted as S1) and samples annealed at 900 °C (S2) and 1100 °C (S3) were studied. As shown in the inset of Fig. 1, TaReSi crystallizes in an orthorhombic structure with a space group of $Ima2$ (No. 46) [54]. All samples were characterized by electrical-resistivity and magnetization measurements, performed on a Quantum Design physical property measurement system (PPMS) and a magnetic property measurement system (MPMS), respectively. The bulk μSR measurements were carried out at the multipurpose surface-muon spectrometer (Dolly) on the πE1 beamline of the Swiss muon source at Paul Scherrer Institut, Villigen, Switzerland. The samples were mounted on a 25-μm-thick copper foil which ensures thermalization at low temperatures. The time-differential μSR data were collected upon heating and then analyzed by means of the musrfit software package [55].

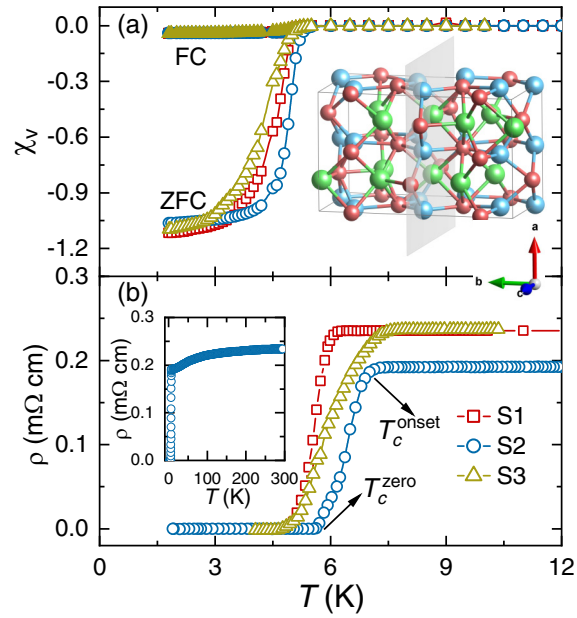

FIG. 1. The temperature-dependent volume magnetic susceptibility $\chi_V(T)$ (a) and electrical resistivity $\rho(T)$ (b) for TaReSi. The results of an as-cast sample (S1) and of samples annealed at 900 °C (S2) and 1100 °C (S3) are shown. While $\rho(T)$ was measured in a zero-field condition, $\chi_V(T)$ data were collected in a magnetic field of 1 mT. The susceptibility data were corrected to account for the demagnetization factor. The inset in (a) shows the crystal structure of TaReSi viewed along the c axis and its mirror plane, while the black lines mark the unit cell. Green, blue, and red spheres are Ta, Re, and Si atoms, respectively. The inset in (b) shows the $\rho(T)$ of S2 up to 300 K.

First-principles calculations were performed based on the density functional theory (DFT), as implemented in the Quantum ESPRESSO package [56,57]. The exchange-correlation function was treated with the generalized gradient approximation using the Perdew-Burke-Ernzerhof (PBE) realization [58]. The projector augmented wave pseudopotentials were adopted [59]. We considered 13 electrons for Ta ($5s^26s^25p^65d^3$), 15 electrons for Re ($5s^26s^25p^65d^5$), and 4 electrons for Si ($3s^23p^2$) as valence electrons. The calculations use the measured lattice parameters $a = 7.002$ Å, $b = 11.614$ Å, and $c = 6.605$ Å, and coordinates Ta_1 (0.2500, 0.2004, 0.2964), Ta_2 (0.2500, 0.7793, 0.2707), Ta_3 (0.2500, 0.9979, 0.9178), Re_1 (0, 0, 0.25), Re_2 (0.0295, 0.3764, 0.1200), and Si_1 (0.25, 0.9747, 0.5055), Si_2 (0.0060, 0.1675, 0.9953) for TaReSi and include also the spin-orbit coupling effects [53]. The kinetic energy cutoff for the wave functions was set to 60 Ry, while for the charge density it was fixed

to 600 Ry. For the self-consistent calculations, the Brillouin zone integration was performed on a Monkhorst-Pack grid mesh of $10\times10\times10\,k$ points, which ensures their unbiased sampling. The convergence criterion was set to 10^{-7} Ry. The Hf and W doping effects were simulated by the virtual crystal approximation (VCA) [60] implemented in the Vienna *Ab initio* Simulation Package (VASP) [61,62].

III. RESULTS AND DISCUSSION

The bulk superconductivity of the TaReSi samples was first characterized by magnetic-susceptibility measurements, using both field-cooling (FC) and zero-field-cooling (ZFC) protocols in an applied magnetic field of 1 mT. As shown in Fig. 1(a), a clear diamagnetic response appears below the superconducting transition at $T_c = 5.5$ K for S2. The samples S1 and S3 show a slightly lower transition temperature, i.e., T_c∼5.0 K. After accounting for the demagnetization factor, the superconducting shielding fraction of TaReSi samples is close to 100%, indicative of bulk SC.

The temperature-dependent electrical resistivity $\rho(T)$ of TaReSi samples was measured from 2 K up to room temperature. It reveals a metallic behavior, without any anomalies associated with structural, magnetic, or charge-density-wave transitions at temperatures above T_c [see lower inset in Fig. 1(b)]. The electrical resistivity in the low-T region is plotted in Fig. 1(b), clearly showing the superconducting transition of all the samples. A $T_c^{\rm onset} = 6.1$, 7.0, and 7.5 K, and $T_c^{\rm zero} = 4.8$, 5.6, and 4.6 K were identified for the S1, S2, and S3 samples, respectively. The $T_c^{\rm zero}$ values are consistent with the transition temperatures determined from the magnetic susceptibility [see Fig. 1(a)]. In view of its higher T_c and narrower ΔT_c transition, most of the μSR measurements were performed on the TaReSi sample S2.

To determine the lower critical field H_{c1}, to be exceeded (at least twice) when performing μSR measurements on type-II superconductors, the field-dependent magnetization $M(H)$ of TaReSi was measured at various temperatures. Here, the $M(H)$ data of the S2 sample are shown in Fig. 2(a), with the other samples showing a similar behavior. The estimated H_{c1} values at different temperatures (accounting for a demagnetization factor), determined from the deviations of $M(H)$ from linearity, are summarized in Fig. 2(b). The solid lines are fits to $\mu_0 H_{c1}(T) = \mu_0 H_{c1}(0)[1-(T/T_c)^2]$ and yield the lower critical fields $\mu_0 H_{c1}(0) = 6.6(1)$, 6.4(1), and 5.5(1) mT for S1, S2, and S3 samples, respectively.

To investigate the upper critical field H_{c2} of TaReSi, we measured the temperature-dependent electrical resistivity $\rho(T,H)$ at various applied magnetic fields, as well as the field-dependent magnetization $M(H,T)$ at various temperatures. As shown in Fig. 3(a), upon increasing the magnetic field, the superconducting transition in $\rho(T)$ shifts to lower temperatures. Similarly, in the $M(H)$ data, the diamagnetic signal vanishes once the applied magnetic field exceeds the upper critical field H_{c2} [see inset in Fig. 3(b)]. Figure 4 summarizes the upper critical fields H_{c2} versus the reduced superconducting transition temperatures $T_c/T_c(0)$ for all the TaReSi samples, as identified from the $\rho(T,H)$ and $M(H,T)$ data. To determine the upper critical field at 0 K, the $H_{c2}(T)$ data were analyzed by means of a semiempirical Ginzburg-

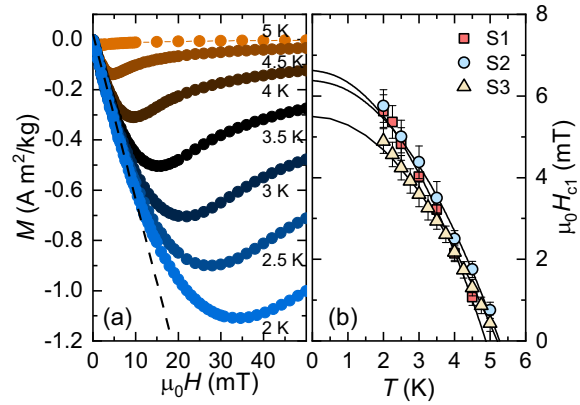

FIG. 2. (a) Field-dependent magnetization curves collected at various temperatures after cooling the S2 sample in zero field (the other samples behave similarly). (b) Lower critical fields H_{c1} vs temperature. Solid lines are fits to $\mu_0 H_{c1}(T) = \mu_0 H_{c1}(0)[1-(T/T_c)^2]$. For each temperature, H_{c1} was determined as the value where $M(H)$ starts deviating from linearity [see dashed line in panel (a)].

Landau (GL) model, $H_{c2} = H_{c2}(0)(1-t^2)/(1+t^2)$, where $t = T/T_c(0)$. As shown by the solid lines, the GL model gives $\mu_0 H_{c2}(0) = 3.7(1)$, 3.4(1), and 3.3(1) T for the TaReSi samples S1, S2, and S3, respectively. As for the electrical-resistivity data, the derived $H_{c2}(0)$ values are much larger than the bulk values determined from magnetization data. The different T_c or H_{c2} values might be related to a strongly

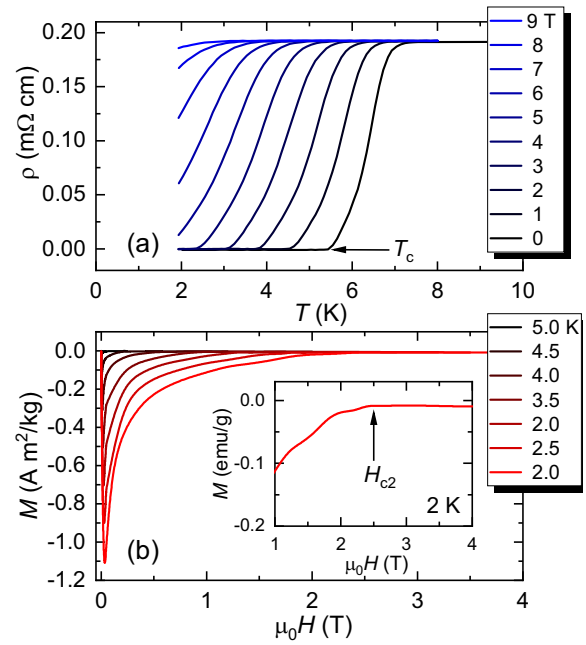

FIG. 3. (a) Temperature-dependent electrical resistivity for various applied magnetic fields. T_c was determined as the onset temperature where the resistivity drops to zero. (b) Field-dependent magnetization (up to 4 T) collected at various temperatures below T_c. The inset shows the high-field range of the $M(H)$ curve at 2 K. H_{c2} was chosen as the field where the diamagnetic response vanishes (indicated by an arrow). The reported data refer to the sample S2; samples S1 and S3 show similar features.

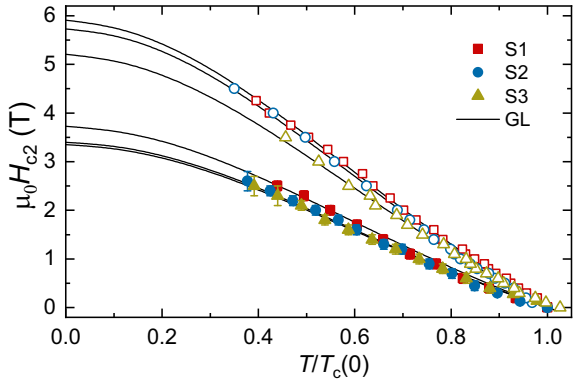

FIG. 4. Upper critical field H_{c2} vs the reduced temperature $T/T_c(0)$ for the different TaReSi samples. The T_c and H_{c2} values were determined from the measurements shown in Fig. 3. Full symbols refer to magnetization, while empty symbols to resistivity measurements. Note the systematically higher values in the latter case. Solid lines represent fits to the GL model.

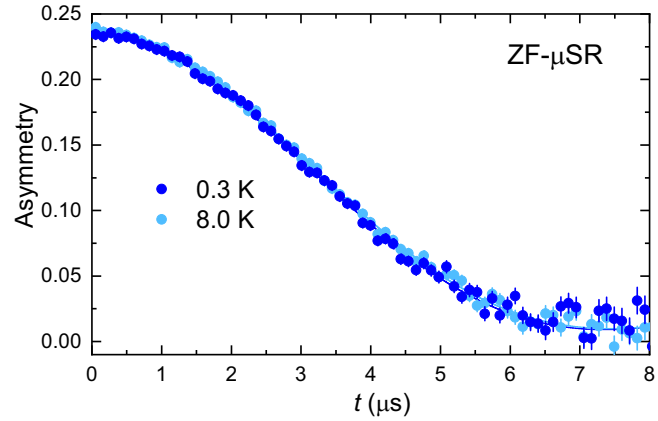

FIG. 5. ZF-μSR spectra collected in the superconducting (0.3 K) and in the normal state (8 K) of TaReSi. The practically overlapping data sets indicate the absence of TRS breaking, whose occurrence would have resulted in a stronger decay in the 0.3 K case.

anisotropic upper critical field, or to the appearance of surface/filamentary superconductivity above bulk T_c. Moreover, although the magnetization and electrical-resistivity measurements reveal different sample qualities, the superconducting properties of TaReSi seem to be robust. Such an insensitivity of SC to nonmagnetic impurities or disorder implies an s-wave pairing in TaReSi, as further evidenced by the μSR measurements (see below).

In the GL theory of superconductivity, the coherence length ξ can be calculated from $\xi = \sqrt{\Phi_0/2\pi H_{c2}}$, where $\Phi_0 = 2.07\times10^3$ T nm^2 is the quantum of magnetic flux. With a bulk $\mu_0 H_{c2}(0) = 3.4(1)$ T (for S2 sample), the calculated $\xi(0)$ is 9.8(1) nm. The magnetic penetration depth λ is related to the coherence length ξ and the lower critical field $\mu_0 H_{c1}$ via $\mu_0 H_{c1} = (\Phi_0/4\pi\lambda^2)[\ln(\kappa) + 0.5]$, where $\kappa = \lambda/\xi$ is the GL parameter [63]. By using $\lambda_0 = 562(3)$ nm, we find $\mu_0 H_{c1} = 2.4(1)$ mT, which is smaller than the value determined from the magnetization data (see Fig. 2). Such difference in H_{c1}, as well as the unusual behavior in H_{c2}, might be attributed to the anisotropic TaReSi superconductivity. To clarify this, studies on the single crystals are required.

Since certain rhenium-based superconductors are known to break time-reversal symmetry in their superconducting state [32–35,64], to verify the possible breaking of TRS in TaReSi, we performed zero-field (ZF) μSR measurements in its normal and superconducting states. This technique is very sensitive to the weak spontaneous fields expected to arise in these cases [64]. As shown in Fig. 5, the ZF-μSR spectra of TaReSi lack any of the features associated with magnetic order or magnetic fluctuations. Indeed, in the data sets collected above (8 K) and below T_c (0.3 K), neither coherent oscillations nor fast decays could be identified. In the absence of an external magnetic field, the muon-spin relaxation is mainly determined by the randomly oriented nuclear moments. As a consequence, the ZF-μSR spectra can be modeled by means of a phenomenological relaxation function, consisting of a combination of a Gaussian and a Lorentzian Kubo-Toyabe relaxation [65,66], i.e., $A_{ZF} = A_s[\frac{1}{3} + \frac{2}{3}(1-\sigma_{ZF}^2 t^2 - \Lambda_{ZF} t)e^{(-\frac{\sigma_{ZF}^2 t^2}{2} - \Lambda_{ZF} t)}] + A_{bg}$. Here, A_s and A_{bg} are the initial asymmetries for the sample and sample holder, and σ_{ZF} and Λ_{ZF} represent the zero-field Gaussian and Lorentzian relaxation rates, respectively. The solid lines in Fig. 5 are fits to the above equation, yielding $\sigma_{ZF} = 0.231(1)$ μs^{-1} and $\Lambda_{ZF} = 0.005(2)$ μs^{-1} at 8 K and $\sigma_{ZF} = 0.234(1)$ μs^{-1} and $\Lambda_{ZF} = 0.003(2)$ μs^{-1} at 0.3 K. The relaxation rates in the normal and the superconducting states of TaReSi are almost identical, visually confirmed by the overlapping ZF-μSR spectra in Fig. 5. The absence of an additional μSR relaxation below T_c excludes the breaking of TRS in the superconducting state of TaReSi. On the contrary, the enhanced σ_{ZF} below T_c in TaRuSi and NbRuSi provides clear evidence of the occurrence of spontaneous magnetic fields, which break the TRS at the superconducting transition [52,67]. Such a selective occurrence of TRS breaking, observed also in other superconducting families [64], independent of the ASOC, is puzzling and not yet fully understood, clearly demanding further investigations. Future ZF-μSR measurements on the TaRu$_{1-x}$Re$_x$Si series could potentially clarify this issue.

To investigate the superconducting pairing in TaReSi, we carried out systematic temperature-dependent transverse-field (TF) μSR measurements in an applied field of 40 mT. Representative TF-μSR spectra collected in the superconducting and normal states of TaReSi are shown in Fig. 6(a). In the superconducting state (e.g., at 0.3 K), the development of a flux-line lattice (FLL) causes an inhomogeneous field distribution and, thus, it gives rise to an additional damping in the TF-μSR spectra [66]. In such case, the TF-μSR spectra are generally modeled using [68]

$$A_{TF}(t) = \sum_{i=1}^{n} A_i \cos(\gamma_\mu B_i t + \phi) e^{-\sigma_i^2 t^2/2} + A_{bg}\cos(\gamma_\mu B_{bg} t + \phi). \quad (1)$$

Here A_i, A_{bg} and B_i, B_{bg} are the initial asymmetries and local fields sensed by implanted muons in the sample and sample holder, $\gamma_\mu/2\pi = 135.53$ MHz/T is the muon gyromagnetic ratio, ϕ is a shared initial phase, and σ_i

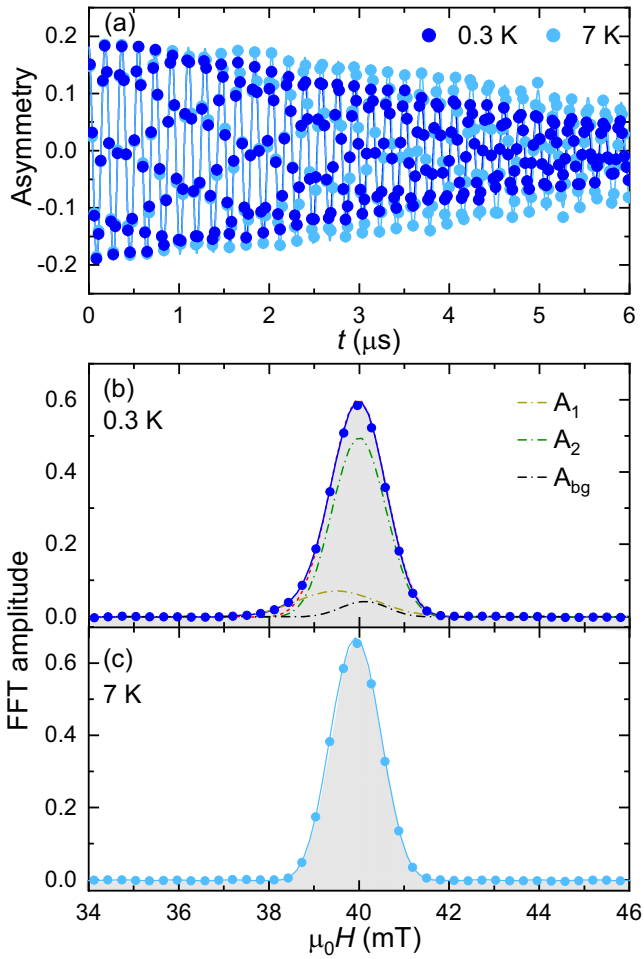

FIG. 6. (a) TF-μSR spectra of TaReSi collected in the superconducting (0.3 K) and normal (7 K) states in an applied magnetic field of 40 mT. Dashed and solid lines are fits to Eq. (1) using one and two oscillations. In the latter case, each contribution is shown separately as dash-dotted lines, together with a background contribution. Fits with two oscillations show a goodness-of-fit value $\chi_r^2 \sim 1.0$, smaller than the one-oscillation fits ($\chi_r^2 \sim 1.6$).

is the Gaussian relaxation rate of the ith component. In general, the field distribution $p(B)$ in the superconducting state is material dependent. In case of a symmetric $p(B)$, one oscillation (i.e., $n = 1$) is sufficient to describe the TF-μSR spectra, while for an asymmetric $p(B)$, two or more oscillations (i.e., $n \geqslant 2$) are required. Here, we find that Eq. (1) with $n = 2$ can describe the experimental data quite well [see solid lines in Fig. 6(a)]. The derived muon-spin relaxation rates σ_i are small and temperature-independent in the normal state, but below T_c they start to increase due to the onset of FLL and the increased superfluid density [see inset in Fig. 7]. Then, the effective Gaussian relaxation rate $\sigma_{\rm eff}$ can be calculated from $\sigma_{\rm eff}^2/\gamma_\mu^2 = \sum_{i=1}^{2} A_i [\sigma_i^2/\gamma_\mu^2 - (B_i - \langle B \rangle)^2]/A_{\rm tot}$ [68], where $\langle B \rangle = (A_1 B_1 + A_2 B_2)/A_{\rm tot}$ and $A_{\rm tot} = A_1 + A_2$. Considering the constant nuclear relaxation rate $\sigma_{\rm n}$ in the narrow temperature range investigated here, confirmed also by ZF-μSR measurements

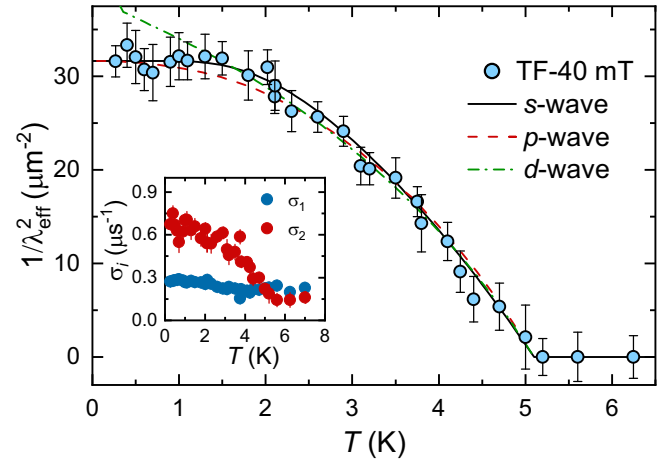

FIG. 7. Temperature dependence of the superfluid density of TaReSi. The inset shows the muon-spin relaxation rates $\sigma_i(T)$ vs temperature. The solid, dashed, and dash-dotted lines represent fits to the s-, p-, and d-wave model, with $\chi_r^2 \sim 1.1$, 1.8, and 5.2, respectively.

(see Fig. 5), the superconducting Gaussian relaxation rate can be extracted using $\sigma_{\rm sc} = \sqrt{\sigma_{\rm eff}^2 - \sigma_{\rm n}^2}$.

In TaReSi, the upper critical field $\mu_0 H_{c2}(0) \sim 3.4$ T is significantly larger than the applied TF field (40 mT). Hence, we can ignore the effects of the overlapping vortex cores when extracting the magnetic penetration depth from the measured $\sigma_{\rm sc}$. The effective magnetic penetration depth $\lambda_{\rm eff}$ can then be calculated by using $\sigma_{\rm sc}^2(T)/\gamma_\mu^2 = 0.00371\Phi_0^2/\lambda_{\rm eff}^4(T)$ [63,69]. Figure 7 summarizes the temperature-dependent inverse square of magnetic penetration depth, which is proportional to the superfluid density, i.e., $\lambda_{\rm eff}^{-2}(T) \propto \rho_{\rm sc}(T)$. The $\rho_{\rm sc}(T)$ was analyzed by applying different models, generally described by

$$\rho_{\rm sc}(T) = 1 + 2\left\langle \int_{\Delta_{\rm k}}^{\infty} \frac{E}{\sqrt{E^2 - \Delta_{\rm k}^2}} \frac{\partial f}{\partial E} dE \right\rangle_{\rm FS}. \qquad (2)$$

Here, $f = (1 + e^{E/k_{\rm B}T})^{-1}$ is the Fermi function and $\langle\,\rangle_{\rm FS}$ represents an average over the Fermi surface (assumed to be an isotropic sphere, for s-wave superconductors) [70]; $\Delta_{\rm k}(T) = \Delta(T)\delta_{\rm k}$ is an angle-dependent gap function, where Δ is the maximum gap value and $\delta_{\rm k}$ is the angular dependence of the gap, equal to 1, $\cos 2\phi$, and $\sin\theta$ for an s-, d-, and p-wave model, respectively, with ϕ and θ being the azimuthal angles. The temperature dependence of the gap is assumed to follow $\Delta(T) = \Delta_0 \tanh\{1.82[1.018(T_c/T - 1)]^{0.51}\}$ [70,71], where Δ_0 is the gap value at 0 K. Three different models, including s-, p-, and d-wave ones, were used to describe the $\lambda_{\rm eff}^{-2}(T)$ data. For an s- or p-wave model [see solid and dashed lines in Fig. 7], the best fits yield the same zero-temperature magnetic penetration depth $\lambda_0 = 562(3)$ nm, but different superconducting gaps $\Delta_0 = 0.79(2)$ and 1.05(2) meV, respectively, while for the d-wave model, the gap size is the same as the p-wave model, but the $\lambda_0 = 510(3)$ nm is much shorter. As can be seen in Fig. 7, the temperature-independent $\lambda_{\rm eff}^{-2}(T)$ for $T < 2$ K strongly suggests a fully gapped superconducting state in TaReSi. As a consequence,

$\lambda_{\rm eff}^{-2}(T)$ is more consistent with the s-wave model, here reflected in the smallest $\chi_{\rm r}^2$. In the case of a p- or d-wave model, a less-good agreement with the measured $\lambda_{\rm eff}^{-2}(T)$ is found, especially at low temperatures. Although the unitary $(s+ip)$ pairing [52] can also describe the nodeless SC in TaReSi, its preserved TRS excludes such a possibility. In summary, TF-μSR combined with ZF-μSR data, indicate that TaReSi behaves as a conventional fully gapped superconductor with preserved TRS.

We also note that due to the lack of inversion symmetry in TaReSi, a mixing of spin-singlet and spin-triplet pairing is allowed. Such mixing not only can be consistent with a fully gapped superconducting state but, more importantly, it can lead to unconventional or even topological SC. Indeed, our TF-μSR results clearly suggests a fully gapped superconducting state, here fitted by using an s-wave model (see Fig. 7). However, this does not imply that s-wave pairing is the only possibility. Mixed singlet-triplet pairings also allow for a fully gapped superconducting state, which in principle is allowed by the presence of ASOC [72]. Furthermore, topological SC can occur when the pairing gap changes sign on different Fermi surfaces according to the topological criterion [73]. For a minimal single-band model, there are two spin-split Fermi surfaces, whose gaps are given by $\Delta_{\rm s} \pm \Delta_{\rm t}(k_{\rm F})$, which implies that a sign change occurs when $\Delta_{\rm s} < \Delta_{\rm t}(k_{\rm F})$.

To gain further insight into the electronic properties of the TaReSi superconductor, we also performed band-structure calculations using the density-functional theory. The electronic band structure of TaReSi and its density of states (DOS) are summarized in Fig. 8. Close to the Fermi level $E_{\rm F}$, the DOS is dominated by the Ta- and Re-5d orbitals, while the contribution from Si-3p orbitals is negligible. The dominance of high-Z orbitals might lead to a relatively large band splitting. In TaReSi, the estimated DOS at $E_{\rm F}$ is about 1.1 states/(eV f.u.) [$=$ 6.5 states/(eV cell)/Z, with $Z = 6$ the number of atoms per primitive cell]. This is comparable to the experimental value of 2.3 states/(eV f.u.), determined from the electronic specific-heat coefficient [54]. The electronic band structure of TaReSi, calculated by ignoring and by considering the spin-orbit coupling, is shown in Fig. 8(b). When taking SOC into account, the electronic bands split due to the lifting of degeneracy, with one of them ending up closer to the Fermi level. The band splitting $E_{\rm ASOC}$ caused by the ASOC is clearly visible in TaReSi, e.g., near the X (X_1), Y, and W points. The estimated band splitting in TaReSi is $E_{\rm ASOC}\sim$300 meV, which is much larger than that of NbRuSi ($\sim$100 meV), but comparable to TaRuSi ($\sim$300 meV) [52]. Though smaller than the band splitting in $CePt_3Si$ [74], it is comparable to that of CaPtAs and Li_2Pt_3B [24,75], and much larger than that of most other weakly correlated NCSCs [19]. The $E_{\rm ASOC}$ of TaReSi is almost twice larger than that of the analog NbReSi compound ($E_{\rm ASOC}\sim$150 meV) [28,76]. The latter crystallizes in a ZrNiAl-type noncentrosymmetric structure ($P\bar{6}2m$, No. 189) and exhibits features of unconventional superconductivity; e.g., its $H_{\rm c2}$ exceeds the Pauli limit. However, the $H_{\rm c2}$ of TaReSi is much smaller than that of NbReSi, the former being mostly determined by the orbital limit. Since Ta has a much larger atomic number than Nb (and, hence, a larger SOC), it is not surprising that TaReSi exhibits a larger $E_{\rm ASOC}$, in particular, considering that its Ta-5d (instead of Nb-4d) orbitals contribute as much as Re-5d orbitals to the DOS at the Fermi energy [see Fig. 8(a)].

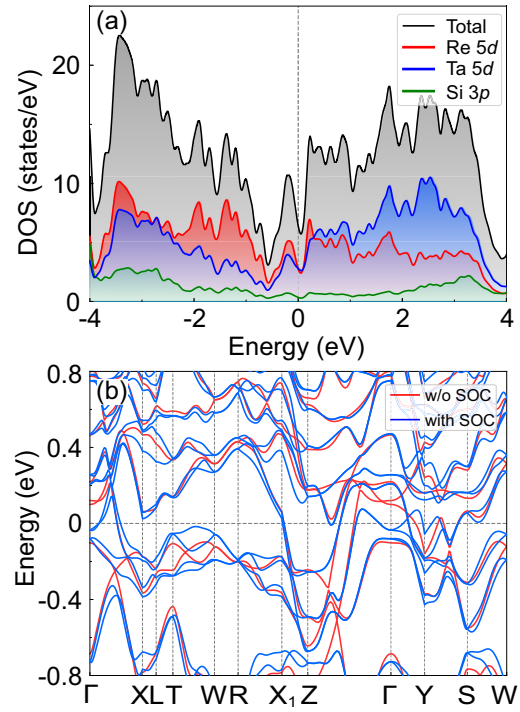

FIG. 8. (a) Calculated total and partial (Ta-5d, Re-5d, and Si-3p orbitals) density of states for TaReSi. (b) Electronic band structure of TaReSi, calculated by ignoring (red) and by considering (blue) the spin-orbit coupling. Several bands crossing the Fermi level can be identified.

According to the Topological Materials Database [5–7,77–79] and from our own band-structure calculations, TaReSi can be classified as a symmetry-enforced semimetal, which shares a similar band topology with NbRuSi and TaRuSi [52]. In the presence of spin-orbit coupling, owing to its nonsymmorphic space group ($Ima2$, No. 46), TaReSi hosts Kramers Weyl points (KWPs) at the high-symmetry points and Kramers nodal lines along the high-symmetry lines of its Brillouin zone. These features are marked by red circles (KWPs) and green/orange lines (KNLs) in Fig. 9(a). The high-symmetry points at S and T are time-reversal symmetry invariant. As a consequence, the respective energies exhibit a twofold Kramers degeneracy protected by TRS. At the same time, due to the lack of inversion symmetry in TaReSi, these points cannot achieve the fourfold degeneracy of Dirac points and, hence, they are Weyl points. As for the high-symmetry lines along the Γ-Z and R-W directions, the bands form a two-dimensional representation, i.e., twofold degenerate, indicating the occurrence of KNLs in TaReSi. Since most of KNLs occur near the $E_{\rm F}$, with a few of them even crossing it, similarly to NbRuSi and TaRuSi [52], TaReSi can be classified as a Kramers nodal-line semimetal (KNLS). At the high-symmetry S and T points, the KWPs in TaReSi are closer to $E_{\rm F}$ than in NbRuSi and TaRuSi [52]. Since the Ru atoms have one more electron than Re, the KWPs in NbRuSi and TaRuSi are shifted further below $E_{\rm F}$.

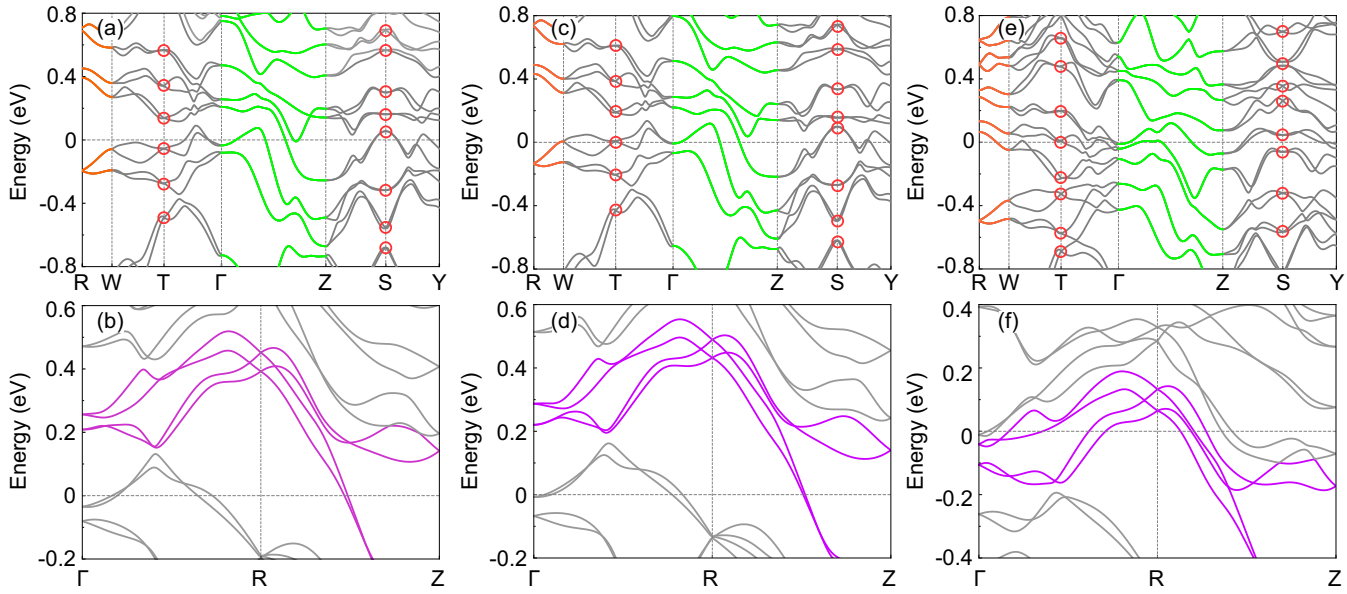

FIG. 9. (a) Illustration of Kramers Weyl points and Kramers nodal lines in TaReSi. The KWPs are marked by red circles, while the KNLs are depicted by green (along $\Gamma-Z$) or orange lines (along $R-W$). (b) Illustration of hourglass-shaped dispersion (purple lines) for TaReSi along the $\Gamma-R-Z$ direction. The analogous results for TaReSi doped with 5% Hf and 50% W are shown in panels (c)–(d) and (e)–(f), respectively.

More interestingly, as shown by purple lines in Fig. 9(b), due to its nonsymmorphic space-group symmetry, TaReSi also exhibits 3D bulk hourglass-type fermions, characterized by an hourglass cone with five doubly degenerate points [13,15]. The $Ima2$ nonsymmorphic space group contains the generator of a glide mirror reflection $M_y = \{m_{010}|1/2, 0, 0\}$: $(x, y, z) \rightarrow (x + 1/2, -y, z)$ [see inset in Fig. 1(a)]. Here, the $k_y = 0$ and π planes are M_y-invariant planes, where all the states along the $\Gamma-R-Z$ line carry the M_y index $\pm ie^{-ik_x/2}$ and give rise to the 3D bulk hourglass fermions, protected by the M_y operator [80,81]. In this case, at a high-symmetry point, the $\mathbf{k}$ vectors are $\mathbf{k}_\Gamma = (0, 0, 0)$, $\mathbf{k}_R = (0, 1/2, 0)$, and $\mathbf{k}_Z = (1/2, 1/2, -1/2)$. Therefore, the M_y index is ± 1 at the R point, and $\pm i$ at the Γ and Z points. In agreement with the Kramers theorem, each state is twofold degenerate; i.e., pairs of doubly degenerate states exhibit identical energies, but carry opposite M_y indexes. In the presence of a strong SOC, these doubly degenerate states split along the $R \rightarrow \Gamma$ or $R \rightarrow Z$ directions. Despite this SOC-induced splitting of bands with different M_y indexes, a residual degeneracy remains, which could give rise to the noninteracting hourglass fermions in TaReSi. To date, hourglass fermions were experimentally observed only in very few materials, as e.g., the KHgSb and $Nb_3(Si, Ge)Te_6$ topological insulators [82,83]. Here, we establish that similarly to the NbRuSi and TaRuSi compounds [52], also TaReSi belongs to this restricted class of materials, where Kramers Weyl points and hourglass fermions exist and can be tuned toward E_F by Hf or W chemical substitutions on the Ta site [see Figs. 9(c) and 9(d) for 5%-Hf substitution and Figs. 9(e) and 9(f) for 50%-W substitution]. At the same time, we could show that neither chemical substitution on the Si site (here introduced via Si-to-Ge substitution) nor physical pressure have appreciable effects on the band structure of TaReSi. Besides exhibiting nontrivial electronic bands, TaReSi shows also intrinsic SC at low temperatures. This remarkable combination makes it a promising candidate material for investigating topological superconducting properties.

IV. CONCLUSION

To summarize, we studied the noncentrosymmetric TaReSi superconductor by means of μSR measurements and band-structure calculations. The superconducting state of TaReSi is characterized by a T_c of $\sim$5.5 K and an upper critical field $\mu_0 H_{c2}(0)$ of $\sim$3.4 T. The temperature-dependent superfluid density reveals a *fully gapped* superconducting state in TaReSi. The lack of spontaneous magnetic fields below T_c indicates a *preserved* time-reversal symmetry in the superconducting state of TaReSi. Electronic band-structure calculations reveal that TaReSi shares a similar band topology to NbRuSi and TaRuSi, which also belong to the three-dimensional Kramers nodal-line semimetals. It, too, features hourglass fermions, protected by the nonsymmorphic space-group symmetry. Our results demonstrate that TaReSi represents a potentially interesting system for investigating the rich interplay between the exotic electronic states of Kramers nodal-line fermions, hourglass fermions, and superconductivity. It will be also interesting to explore the Zeeman-field-induced Weyl superconductor in this material. Considering the nontrivial band structure near the Fermi level and its intrinsic superconductivity, TaReSi represents one of the promising platforms for investigating the topological aspects of noncentrosymmetric superconductors.

ACKNOWLEDGMENTS

This work was supported by the Natural Science Foundation of Shanghai (Grants No. 21ZR1420500 and No.

21JC1402300), the Natural Science Foundation of Chongqing (Grant No. CSTB2022NSCQ-MSX1678), and the Schweizerische Nationalfonds zur Förderung der Wissenschaftlichen Forschung (SNF) (Grants No. 200021_188706 and No. 206021_139082). Y.X. acknowledges support from the Shanghai Pujiang Program (Grant No. 21PJ1403100). We acknowledge the allocation of beam time at the Swiss muon source (Dolly μSR spectrometer).

[1] N. P. Armitage, E. J. Mele, and A. Vishwanath, Weyl and Dirac semimetals in three-dimensional solids, Rev. Mod. Phys. **90**, 015001 (2018).

[2] B. Q. Lv, T. Qian, and H. Ding, Experimental perspective on three-dimensional topological semimetals, Rev. Mod. Phys. **93**, 025002 (2021).

[3] B. Yan and C. Felser, Topological materials: Weyl semimetals, Annu. Rev. Condens. Matter Phys. **8**, 337 (2017).

[4] B. J. Wieder, B. Bradlyn, J. Cano, Z. Wang, M. G. Vergniory, L. Elcoro, A. A. Soluyanov, C. Felser, T. Neupert, N. Regnault, and B. A. Bernevig, Topological materials discovery from crystal symmetry, Nat. Rev. Mater. **7**, 196 (2022).

[5] B. Bradlyn, L. Elcoro, J. Cano, M. G. Vergniory, Z. Wang, C. Felser, M. I. Aroyo, and B. A. Bernevig, Topological quantum chemistry, Nature (London) **547**, 298 (2017).

[6] M. G. Vergniory, L. Elcoro, C. Felser, N. Regnault, B. A. Bernevig, and Z. Wang, A complete catalogue of high-quality topological materials, Nature (London) **566**, 480 (2019).

[7] F. Tang, H. C. Po, A. Vishwanath, and X. Wan, Comprehensive search for topological materials using symmetry indicators, Nature (London) **566**, 486 (2019).

[8] B. A. Bernevig, C. Felser, and H. Beidenkopf, Progress and prospects in magnetic topological materials, Nature (London) **603**, 41 (2022).

[9] S.-Y. Xu, I. Belopolski, N. Alidoust, M. Neupane, G. Bian, C. Zhang, R. Sankar, G. Chang, Z. Yuan, C.-C. Lee, S.-M. Huang, H. Zheng, J. Ma, D. S. Sanchez, B. Wang, A. Bansil, F. Chou, P. P. Shibayev, H. Lin, S. Jia *et al.*, Discovery of a Weyl fermion semimetal and topological Fermi arcs, Science **349**, 613 (2015).

[10] S.-Y. Xu, N. Alidoust, I. Belopolski, Z. Yuan, G. Bian, T.-R. Chang, H. Zheng, V. N. Strocov, D. S. Sanchez, G. Chang *et al.*, Discovery of a Weyl fermion state with Fermi arcs in niobium arsenide, Nat. Phys. **11**, 748 (2015).

[11] B. Q. Lv, H. M. Weng, B. B. Fu, X. P. Wang, H. Miao, J. Ma, P. Richard, X. C. Huang, L. X. Zhao, G. F. Chen, Z. Fang, X. Dai, T. Qian, and H. Ding, Experimental Discovery of Weyl Semimetal TaAs, Phys. Rev. X **5**, 031013 (2015).

[12] N. Xu, H. M. Weng, B. Q. Lv, C. E. Matt, J. Park, F. Bisti, V. N. Strocov, D. Gawryluk, E. Pomjakushina, K. Conder, N. C. Plumb, M. Radovic, G. Autés, O. V. Yazyev, Z. Fang, X. Dai, T. Qian, J. Mesot, H. Ding, and M. Shi, Observation of Weyl nodes and Fermi arcs in tantalum phosphide, Nat. Commun. **7**, 11006 (2016).

[13] Z. Wang, A. Alexandradinata, R. J. Cava, and B. A. Bernevig, Hourglass fermions, Nature (London) **532**, 189 (2016).

[14] W. Wu, Y. Jiao, S. Li, X.-L. Sheng, Z.-M. Yu, and S. A. Yang, Hourglass Weyl loops in two dimensions: Theory and material realization in monolayer GaTeI family, Phys. Rev. Mater. **3**, 054203 (2019).

[15] L. Wu, F. Tang, and X. Wan, Exhaustive list of topological hourglass band crossings in 230 space groups, Phys. Rev. B **102**, 035106 (2020).

[16] G. Chang, B. J. Wieder, F. Schindler, D. S. Sanchez, I. Belopolski, S.-M. Huang, B. Singh, D. Wu, T.-R. Chang, T. Neupert, S.-Y. Xu, H. Lin, and M. Z. Hasan, Topological quantum properties of chiral crystals, Nat. Mater. **17**, 978 (2018).

[17] Y.-M. Xie, X.-J. Gao, X. Y. Xu, C.-P. Zhang, J.-X. Hu, J. Z. Gao, and K. T. Law, Kramers nodal line metals, Nat. Commun. **12**, 3064 (2021).

[18] *Non-Centrosymmetric Superconductors*, edited by E. Bauer and M. Sigrist, Lecture Notes in Physics Vol. 847 (Springer Verlag, Berlin, 2012).

[19] M. Smidman, M. B. Salamon, H. Q. Yuan, and D. F. Agterberg, Superconductivity and spin-orbit coupling in noncentrosymmetric materials: A review, Rep. Prog. Phys. **80**, 036501 (2017).

[20] S. K. Ghosh, M. Smidman, T. Shang, J. F. Annett, A. D. Hillier, J. Quintanilla, and H. Yuan, Recent progress on superconductors with time-reversal symmetry breaking, J. Phys.: Condens. Matter **33**, 033001 (2021).

[21] H. Q. Yuan, D. F. Agterberg, N. Hayashi, P. Badica, D. Vandervelde, K. Togano, M. Sigrist, and M. B. Salamon, *s*-Wave Spin-Triplet Order in Superconductors without Inversion Symmetry: Li_2Pd_3B and Li_2Pt_3B, Phys. Rev. Lett. **97**, 017006 (2006).

[22] M. Nishiyama, Y. Inada, and G.-Q. Zheng, Spin Triplet Superconducting State Due to Broken Inversion Symmetry in Li_2Pt_3B, Phys. Rev. Lett. **98**, 047002 (2007).

[23] I. Bonalde, W. Brämer-Escamilla, and E. Bauer, Evidence for Line Nodes in the Superconducting Energy Gap of Noncentrosymmetric $CePt_3Si$ from Magnetic Penetration Depth Measurements, Phys. Rev. Lett. **94**, 207002 (2005).

[24] T. Shang, M. Smidman, A. Wang, L.-J. Chang, C. Baines, M. K. Lee, Z. Y. Nie, G. M. Pang, W. Xie, W. B. Jiang, M. Shi, M. Medarde, T. Shiroka, and H. Q. Yuan, Simultaneous Nodal Superconductivity and Time-Reversal Symmetry Breaking in the Noncentrosymmetric Superconductor CaPtAs, Phys. Rev. Lett. **124**, 207001 (2020).

[25] S. Kuroiwa, Y. Saura, J. Akimitsu, M. Hiraishi, M. Miyazaki, K. H. Satoh, S. Takeshita, and R. Kadono, Multigap Superconductivity in Sesquicarbides La_2C_3 and Y_2C_3, Phys. Rev. Lett. **100**, 097002 (2008).

[26] E. M. Carnicom, W. Xie, T. Klimczuk, J. J. Lin, K. Górnicka, Z. Sobczak, N. P. Ong, and R. J. Cava, $TaRh_2B_2$ and $NbRh_2B_2$: Superconductors with a chiral noncentrosymmetric crystal structure, Sci. Adv. **4**, eaar7969 (2018).

[27] E. Bauer, G. Hilscher, H. Michor, C. Paul, E. W. Scheidt, A. Gribanov, Y. Seropegin, H. Noël, M. Sigrist, and P. Rogl, Heavy Fermion Superconductivity and Magnetic Order in Noncentrosymmetric $CePt_3Si$, Phys. Rev. Lett. **92**, 027003 (2004).

[28] H. Su, T. Shang, F. Du, C. F. Chen, H. Q. Ye, X. Lu, C. Cao, M. Smidman, and H. Q. Yuan, NbReSi: A noncentrosymmetric superconductor with large upper critical field, Phys. Rev. Mater. **5**, 114802 (2021).

[29] A. D. Hillier, J. Quintanilla, and R. Cywinski, Evidence for Time-Reversal Symmetry Breaking in the Noncentrosymmetric Superconductor $LaNiC_2$, Phys. Rev. Lett. **102**, 117007 (2009).

[30] J. A. T. Barker, D. Singh, A. Thamizhavel, A. D. Hillier, M. R. Lees, G. Balakrishnan, D. M. Paul, and R. P. Singh, Unconventional Superconductivity in La_7Ir_3 Revealed by Muon Spin Relaxation: Introducing a New Family of Noncentrosymmetric Superconductor That Breaks Time-Reversal Symmetry, Phys. Rev. Lett. **115**, 267001 (2015).

[31] T. Shang, S. K. Ghosh, J. Z. Zhao, L.-J. Chang, C. Baines, M. K. Lee, D. J. Gawryluk, M. Shi, M. Medarde, J. Quintanilla, and T. Shiroka, Time-reversal symmetry breaking in the noncentrosymmetric Zr_3Ir superconductor, Phys. Rev. B **102**, 020503(R) (2020).

[32] R. P. Singh, A. D. Hillier, B. Mazidian, J. Quintanilla, J. F. Annett, D. M. Paul, G. Balakrishnan, and M. R. Lees, Detection of Time-Reversal Symmetry Breaking in the Noncentrosymmetric Superconductor Re_6Zr Using Muon-Spin Spectroscopy, Phys. Rev. Lett. **112**, 107002 (2014).

[33] T. Shang, G. M. Pang, C. Baines, W. B. Jiang, W. Xie, A. Wang, M. Medarde, E. Pomjakushina, M. Shi, J. Mesot, H. Q. Yuan, and T. Shiroka, Nodeless superconductivity and time-reversal symmetry breaking in the noncentrosymmetric superconductor $Re_{24}Ti_5$, Phys. Rev. B **97**, 020502(R) (2018).

[34] T. Shang, M. Smidman, S. K. Ghosh, C. Baines, L. J. Chang, D. J. Gawryluk, J. A. T. Barker, R. P. Singh, D. M. Paul, G. Balakrishnan, E. Pomjakushina, M. Shi, M. Medarde, A. D. Hillier, H. Q. Yuan, J. Quintanilla, J. Mesot, and T. Shiroka, Time-Reversal Symmetry Breaking in Re-Based Superconductors, Phys. Rev. Lett. **121**, 257002 (2018).

[35] T. Shang, C. Baines, L.-J. Chang, D. J. Gawryluk, E. Pomjakushina, M. Shi, M. Medarde, and T. Shiroka, $Re_{1-x}Mo_x$ as an ideal test case of time-reversal symmetry breaking in unconventional superconductors, npj Quantum Mater. **5**, 76 (2020).

[36] M. Sato and Y. Ando, Topological superconductors: A review, Rep. Prog. Phys. **80**, 076501 (2017).

[37] X.-L. Qi and S.-C. Zhang, Topological insulators and superconductors, Rev. Mod. Phys. **83**, 1057 (2011).

[38] C. Kallin and J. Berlinsky, Chiral superconductors, Rep. Prog. Phys. **79**, 054502 (2016).

[39] H. Kim, K. Wang, Y. Nakajima, R. Hu, S. Ziemak, P. Syers, L. Wang, H. Hodovanets, J. D. Denlinger, P. M. R. Brydon, D. F. Agterberg, M. A. Tanatar, R. Prozorov, and J. Paglione, Beyond triplet: Unconventional superconductivity in a spin-3/2 topological semimetal, Sci. Adv. **4**, eaao4513 (2018).

[40] Z. X. Sun, M. Enayat, A. Maldonado, C. Lithgow, E. Yelland, D. C. Peets, A. Yaresko, A. P. Schnyder, and P. Wahl, Dirac surface states and nature of superconductivity in noncentrosymmetric BiPd, Nat. Commun. **6**, 6633 (2015).

[41] M. N. Ali, Q. D. Gibson, T. Klimczuk, and R. J. Cava, Noncentrosymmetric superconductor with a bulk three-dimensional Dirac cone gapped by strong spin-orbit coupling, Phys. Rev. B **89**, 020505(R) (2014).

[42] M. Sato and S. Fujimoto, Topological phases of noncentrosymmetric superconductors: Edge states, Majorana fermions, and non-Abelian statistics, Phys. Rev. B **79**, 094504 (2009).

[43] Y. Tanaka, Y. Mizuno, T. Yokoyama, K. Yada, and M. Sato, Anomalous Andreev Bound State in Noncentrosymmetric Superconductors, Phys. Rev. Lett. **105**, 097002 (2010).

[44] L. Fu and C. L. Kane, Superconducting Proximity Effect and Majorana Fermions at the Surface of a Topological Insulator, Phys. Rev. Lett. **100**, 096407 (2008).

[45] S.-Y. Xu, N. Alidoust, I. Belopolski, A. Richardella, C. Liu, M. Neupane, G. Bian, S.-H. Huang, R. Sankar, C. Fang, B. Dellabetta, W. Dai, Q. Li, M. J. Gilbert, F. Chou, N. Samarth, and M. Z. Hasan, Momentum-space imaging of Cooper pairing in a half-Dirac-gas topological superconductor, Nat. Phys. **10**, 943 (2014).

[46] J.-P. Xu, C. Liu, M.-X. Wang, J. Ge, Z.-L. Liu, X. Yang, Y. Chen, Y. Liu, Z.-A. Xu, C.-L. Gao, D. Qian, F.-C. Zhang, and J.-F. Jia, Artificial Topological Superconductor by the Proximity Effect, Phys. Rev. Lett. **112**, 217001 (2014).

[47] Y. S. Hor, A. J. Williams, J. G. Checkelsky, P. Roushan, J. Seo, Q. Xu, H. W. Zandbergen, A. Yazdani, N. P. Ong, and R. J. Cava, Superconductivity in $Cu_xBi_2Se_3$ and Its Implications for Pairing in the Undoped Topological Insulator, Phys. Rev. Lett. **104**, 057001 (2010).

[48] S. Sasaki, M. Kriener, K. Segawa, K. Yada, Y. Tanaka, M. Sato, and Y. Ando, Topological Superconductivity in $Cu_xBi_2Se_3$, Phys. Rev. Lett. **107**, 217001 (2011).

[49] P. Zhang, K. Yaji, T. Hashimoto, Y. Ota, T. Kondo, K. Okazaki, Z. Wang, J. Wen, G. D. Gu, H. Ding, and S. Shin, Observation of topological superconductivity on the surface of an iron-based superconductor, Science **360**, 182 (2018).

[50] S.-Y. Guan, P.-J. Chen, M.-W. Chu, R. Sankar, F. Chou, H.-T. Jeng, C.-S. Chang, and T.-M. Chuang, Superconducting topological surface states in the noncentrosymmetric bulk superconductor $PbTaSe_2$, Sci. Adv. **2**, e1600894 (2016).

[51] M. Sakano, K. Okawa, M. Kanou, H. Sanjo, T. Okuda, T. Sasagawa, and K. Ishizaka, Topologically protected surface states in a centrosymmetric superconductor β-$PdBi_2$, Nat. Commun. **6**, 8595 (2015).

[52] T. Shang, J. Zhao, L.-H. Hu, J. Ma, D. J. Gawryluk, X. Zhu, H. Zhang, Z. Zhen, B. Yu, Y. Xu, Q. Zhan, E. Pomjakushina, M. Shi, and T. Shiroka, Unconventional superconductivity in topological Kramers nodal-line semimetals, Sci. Adv. **8**, eabq6589 (2022).

[53] G. V. Subba Rao, K. Wagner, G. Balakrishnan, J. Janaki, W. Paulus, R. Schöllhorn, V. S. Subramanian, and U. Poppe, Structure and superconductivity studies on ternary equiatomic silicides MM'Si, Bull. Mater. Sci. **7**, 215 (1985).

[54] K. P. Sajilesh and R. P. Singh, Superconducting properties of the non-centrosymmetric superconductors TaXSi (X = Re, Ru), Supercond. Sci. Technol. **34**, 055003 (2021).

[55] A. Suter and B. M. Wojek, Musrfit: A free platform-independent framework for μSR data analysis, Phys. Procedia **30**, 69 (2012).

[56] P. Giannozzi, S. Baroni, N. Bonini, M. Calandra, R. Car, C. Cavazzoni, D. Ceresoli, G. L. Chiarotti, M. Cococcioni, I. Dabo, A. D. Corso, S. de Gironcoli, S. Fabris, G. Fratesi, R. Gebauer, U. Gerstmann, C. Gougoussis, A. Kokalj, M. Lazzeri, L. Martin-Samos *et al.*, Quantum ESPRESSO: A modular and open-source software project for quantum simulations of materials, J. Phys.: Condens. Matter **21**, 395502 (2009).

[57] P. Giannozzi, O. Andreussi, T. Brumme, O. Bunau, M. B. Nardelli, M. Calandra, R. Car, C. Cavazzoni, D. Ceresoli, M. Cococcioni, N. Colonna, I. Carnimeo, A. D. Corso, S. de

Gironcoli, P. Delugas, R. A. DiStasio, A. Ferretti, A. Floris, G. Fratesi, G. Fugallo *et al.*, Advanced capabilities for materials modelling with Quantum ESPRESSO, J. Phys.: Condens. Matter **29**, 465901 (2017).

[58] J. P. Perdew, K. Burke, and M. Ernzerhof, Generalized Gradient Approximation Made Simple, Phys. Rev. Lett. **77**, 3865 (1996).

[59] P. E. Blöchl, Projector augmented-wave method, Phys. Rev. B **50**, 17953 (1994).

[60] L. Bellaiche and D. Vanderbilt, Virtual crystal approximation revisited: Application to dielectric and piezoelectric properties of perovskites, Phys. Rev. B **61**, 7877 (2000).

[61] G. Kresse and J. Furthmüller, Efficient iterative schemes for *ab initio* total-energy calculations using a plane-wave basis set, Phys. Rev. B **54**, 11169 (1996).

[62] G. Kresse and J. Furthmüller, Efficiency of ab-initio total energy calculations for metals and semiconductors using a plane-wave basis set, Comput. Mater. Sci. **6**, 15 (1996).

[63] E. H. Brandt, Properties of the ideal Ginzburg-Landau vortex lattice, Phys. Rev. B **68**, 054506 (2003).

[64] T. Shang and T. Shiroka, Time-reversal symmetry breaking in Re-based superconductors: Recent developments, Front. Phys. **9**, 651163 (2021), and references therein.

[65] R. Kubo and T. Toyabe, A stochastic model for low-field resonance and relaxation, in *Magnetic Resonance and Relaxation. Proceedings of the XIVth Colloque Ampère*, edited by R. Blinc (North-Holland, Amsterdam, 1967), pp. 810–823.

[66] A. Yaouanc and P. D. de Réotier, *Muon Spin Rotation, Relaxation, and Resonance: Applications to Condensed Matter* (Oxford University Press, Oxford, 2011).

[67] S. Sharma, K. P. Sajilesh, A. D. S. Richards, J. Gautreau, M. Pula, J. Beare, K. M. Kojima, S. Yoon, Y. Cai, R. K. Kushwaha, T. Agrawal, E. S. Sørensen, R. P. Singh, and G. M. Luke, Role of spin orbital coupling in unconventional superconductivity, arXiv:2209.09852.

[68] A. Maisuradze, R. Khasanov, A. Shengelaya, and H. Keller, Comparison of different methods for analyzing μSR line shapes in the vortex state of type-II superconductors, J. Phys.: Condens. Matter **21**, 075701 (2009), and references therein.

[69] W. Barford and J. M. F. Gunn, The theory of the measurement of the London penetration depth in uniaxial type-II superconductors by muon spin rotation, Phys. C (Amsterdam, Neth.) **156**, 515 (1988).

[70] M. Tinkham, *Introduction to Superconductivity*, 2nd ed. (Dover Publications, Mineola, NY, 1996).

[71] A. Carrington and F. Manzano, Magnetic penetration depth of MgB_2, Phys. C (Amsterdam, Neth.) **385**, 205 (2003).

[72] L.-H. Hu, X. Wang, and T. Shang, Spontaneous magnetization in unitary superconductors with time reversal symmetry breaking, Phys. Rev. B **104**, 054520 (2021).

[73] X.-L. Qi, T. L. Hughes, and S.-C. Zhang, Topological invariants for the Fermi surface of a time-reversal-invariant superconductor, Phys. Rev. B **81**, 134508 (2010).

[74] K. V. Samokhin, E. S. Zijlstra, and S. K. Bose, $CePt_3Si$: An unconventional superconductor without inversion center, Phys. Rev. B **69**, 094514 (2004).

[75] K.-W. Lee and W. E. Pickett, Crystal symmetry, electron-phonon coupling, and superconducting tendencies in Li_2Pd_3B and Li_2Pt_3B, Phys. Rev. B **72**, 174505 (2005).

[76] T. Shang, D. Tay, H. Su, H. Q. Yuan, and T. Shiroka, Evidence of fully gapped superconductivity in NbReSi: A combined μSR and NMR study, Phys. Rev. B **105**, 144506 (2022).

[77] T. Zhang, Y. Jiang, Z. Song, H. Huang, Y. He, Z. Fang, H. Weng, and C. Fang, Catalogue of topological electronic materials, Nature (London) **566**, 475 (2019).

[78] Topological Materials Database, https://topologicalquantumchemistry.org.

[79] Bilbao Crystallographic Server, https://www.cryst.ehu.es.

[80] M. Ezawa, Hourglass fermion surface states in stacked topological insulators with nonsymmorphic symmetry, Phys. Rev. B **94**, 155148 (2016).

[81] L. Wang, S.-K. Jian, and H. Yao, Hourglass semimetals with nonsymmorphic symmetries in three dimensions, Phys. Rev. B **96**, 075110 (2017).

[82] J. Ma, C. Yi, B. Lv, Z. Wang, S. Nie, L. Wang, L. Kong, Y. Huang, P. Richard, P. Zhang, K. Yaji, K. Kuroda, S. Shin, H. Weng, B. A. Bernevig, Y. Shi, T. Qian, and H. Ding, Experimental evidence of hourglass fermion in the candidate nonsymmorphic topological insulator KHgSb, Sci. Adv. **3**, e1602415 (2017).

[83] Q. Wan, T. Y. Yang, S. Li, M. Yang, Z. Zhu, C. L. Wu, C. Peng, S. K. Mo, W. Wu, Z. H. Chen, Y. B. Huang, L. L. Lev, V. N. Strocov, J. Hu, Z. Q. Mao, H. Zheng, J. F. Jia, Y. G. Shi, S. A. Yang, and N. Xu, Inherited weak topological insulator signatures in the topological hourglass semimetal Nb_3XTe_6 (X = Si, Ge), Phys. Rev. B **103**, 165107 (2021).